Supplementary Information for

A versatile spaceborne architecture for immediate monitoring of the global methane pledge

Yuchen Wang[1], Xvli Guo[1], Yajie Huo[1], Mengying Li[2], Yuqing Pan[1*], Shaocai Yu[2*], Alexander Baklanov[3], Daniel Rosenfeld[4], John H. Seinfeld[5], and Pengfei Li[1*]

[1]College of Science and Technology, Hebei Agricultural University, Baoding, Hebei 071000, P.R. China
[2]Research Center for Air Pollution and Health; Key Laboratory of Environmental Remediation and Ecological Health, Ministry of Education, College of Environment and Resource Sciences, Zhejiang University, Hangzhou, Zhejiang 310058, P.R. China
[3]Science and Innovation Department, World Meteorological Organization (WMO), Geneva, Switzerland
[4]Institute of Earth Science, The Hebrew University of Jerusalem, Jerusalem, Israel
[5]Division of Chemistry and Chemical Engineering, California Institute of Technology, Pasadena, CA 91125, USA

[*]*Correspondence to*: Pengfei Li (lpf_zju@163.com)
Shaocai Yu (shaocaiyu@zju.edu.cn)
Yuqing Pan (panyuqing@hebau.edu.cn)

1. Methods for uncertainty analysis

(1) Uncertainties in the PRISMA-based methane retrievals. The PRISMA-based methane retrievals can present systematic and random errors. We thus evaluated their performance using end-to-end simulations, as shown in previous studies. First, the ideal plumes were prescribed via the large-eddy-driven Weather and Research Forecasting Model (the WRF-Chem-LES model)[1]. The key configuration included common wind fields (i.e., 3.5 m/s), high resolution (i.e., 30 ×30 m^2), and constant emission rates (e.g., 500, 1000, and 1500 kg/h). On this basis, uncorrelated noises with random increments were then added. They represented the expected instrument precision presenting normal distributions with zero mean biases and standard deviations of 1 ~ 5 %. Second, the enhancements of volume mixing ratios were converted into two-way spectral atmospheric transmittance. The calculation basis included air mass factors based on the real observation zenith angles, vertical profiles of dry air column densities, and methane absorption cross-section data. These three data came from the satellite instrument records, ERA5 reanalysis dataset, and the HIgh-resolution TRANSmission molecular absorption (HITRAN2016) database. Third, the subsequent transmittance spectra were convolved with the PRISMA-based spectral responses and then multiplied by the original PRISMA top-of-atmosphere radiance spectrums. To prevent across-track variations in spectral calibration, we performed such processes on a per-column basis. Finally, the resulting PRISMA-based top-of-atmosphere radiance images were processed with the same matched-filter algorithm over the cases explored in this work. Methane retrieval results via the WRF-Chem-LES simulations and associated biases were presented in Table S3. Therefore, we did not observe systematic errors in the PRISMA-based methane retrievals. Detailed evaluations are shown in Supplementary Information.

(2) Uncertainties in the TROPOMI-based methane emission estimates. We provided independent emission estimates for the TROPOMI-based methane hotspots using the WRF-Chem model. On this basis, the differences between the WRF-Chem-based and IME-based results reflected the intrinsic uncertainties in the IME method.

The WRF simulation was nudged to National Centers for Environmental Prediction final analysis data at 0.25° × 0.25° spatial resolution and six-hour temporal resolution. For each hotspot, the model was performed at 5 × 5 km^2 horizontal resolution over a 50 × 50 km^2 domain. The boundary condition was obtained from the CAMS reanalysis dataset. Note that the inner domain did not feedback with the outer domain (i.e., so-called one-way nested simulations). The grid-specific methane emissions were originally taken from the bottom-up emission inventories (EDGARv6.0). Other general configurations could be found in our previous studies[2,3].

Methane emissions were estimated via the Bayesian inverse solution which optimized a single state vector $\mathbf{x}$ as:

$$\hat{\mathbf{x}} = \mathbf{x_A} + \mathbf{S_A}\mathbf{K}^{\boldsymbol{T}}(\mathbf{K}\mathbf{S_A}\mathbf{K}^{\boldsymbol{T}} + \mathbf{S_C})^{-\mathbf{1}}(\mathbf{y} - \mathbf{K}\mathbf{x_A}), \text{ (Eq. 6)}$$

where $\hat{\mathbf{x}}$ was the optimized state vector containing individual elements for daily emissions as well as daily background concentrations; $\mathbf{x_A}$ was the prior taken as the mean reported emission rate from the bottom-up emission inventories; $\mathbf{K}$ was the Jacobian constructed by running perturbation simulations for the state vector element; $\mathbf{S_A}$ was the prior error covariance matrix using 100% error for the emissions and10% for the boundary conditions; $\mathbf{y}$ contained the TROPOMI observations; and $\mathbf{S_C}$ was the observational error covariance matrix using as error the standard deviation of the difference between the prior model and the observations (20 ppb).

Because of uncertainties in meteorology, the WRF output sometime before or after the observation time can give a better simulation of the scene. Hence, we sampled model simulations one hour before and after the optimal time at 15-min time intervals. To ensure that small mismatches between the locations in the simulated and TROPOMI-based hotspots do not lead to underestimated emissions, we then averaged TROPOMI pixels together on a 3 × 3 grid before the inversion and estimated the observational error following the central limit theorem (i.e. dividing by $\sqrt{\mathbf{n}}$ where $\mathbf{n}$ is the number of observations).

The IME method can also be constrained by the WRF-Chem-based wind fields. On this basis, the subsequent TROPOMI-based methane emission estimates could be compared with the original IME-based results (i.e., driven by the ERA5 reanalysis data). The resulting differences would reflect the impacts of the wind data on the IME-based methane emission estimates.

From this analysis, we concluded that the TROPOMI-based methane emission estimates based on the IME method were reliable, the errors of which could be controlled within -40% (Table S2). Detailed evaluations are shown in Supplementary Information.

(3) Uncertainties in the PRISMA-based methane emission estimates. We provided independent emission estimates for the PRISMA-based methane plumes using the WRF-Chem-LES model[4]. The differences between the WRF-CHEM-LES-based and IME-based results reflected the intrinsic uncertainties in the IME method. For each plume, this model was conducted at 30 × 30 m^2 horizontal resolution over a 3 × 3 km^2 domain. This resolution and domain size allowed the placement and resolving of the individual plume and kept the computational and storage costs at a reasonable level. Each simulation had 121 vertical levels, with ∼ 3 m for the first three layers and ∼10 m for the upper layers up to the model top at 2 km height. The terrain information in the inner domain was obtained from the United States Geological Survey (http://ned.usgs.gov/) at 1/3 arc-second (∼10 m) resolution representative of the areas where the methane plumes were active. The boundary condition was obtained from a regional CTM (the two-way coupled WRF-CMAQ model) simulation with 3 × 3 km^2 horizontal resolution over a 12 × 12 km^2 domain. Other configurations were shown in our previous results[2,3,5]. Note that the inner domain did not feedback with the outer domain (i.e., so-called one-way nested simulations). This configuration would not affect our results as the simulated plumes would not touch the boundaries of the inner domain. Each simulation was performed for five hours. The first three hours served as a spin-up period, while the rest two hours were used for analysis. The time step for the inner domain is 0.1 s, and instantaneous values were saved every second (i.e., every ten time-steps). Confidence intervals were obtained from the t-statistic calculated every 5 minutes during the simulation, starting from 15 minutes before and ending 15 minutes after the satellite overpass.

For each plume, its nominal emission magnitude was assumed to be 1000 kg/h. On this basis, the emission magnitude was scaled by matching the total mass of excess methane in the simulated plume. The specific grids that the plume covered were defined using the “contourLines” function of R with a custom threshold (i.e., 2.5% of the total mass of excess methane, corresponding to the variance of the scene-based methane retrieval). The identified grids would not be sensitive to the configuration of the threshold due to the sharp plume edge. Meanwhile, the local background was defined within 1 km of the emission source. Finally, we adjusted the scale factor to best match the area-integrated total mass of excess methane of the observed plume. On this basis, the WRF-Chem-LES-based emission estimates were achieved. Collectively, the differences between the WRF-Chem-LES-based and IME-based results reflected the intrinsic uncertainties in the IME method.

The IME method can also be constrained by the WRF-Chem-LES-based wind fields. On this basis, the subsequent PRISMA-based methane emission estimates could be compared with the original IME-based results (i.e., driven by the ERA5 reanalysis data). The resulting differences would reflect the impacts of the wind data on the IME-based methane emission estimates.

From this analysis, we concluded that the PRISMA-based methane emission estimates based on the IME method were reliable, the errors of which could be controlled within -70% (Table S3). Such uncertainties confirmed the precision errors of the estimated $\boldsymbol{Q}$ derived from the propagated errors in $\boldsymbol{U_{10}}$ and $\mathbf{IME}$ (Table S1). Detailed evaluations are shown in Supplementary Information.

Note that such quantitative estimates of the errors were close to previous findings but might be unsuitable worldwide, especially for those occurring in more complex conditions. We thus expected that, as our framework was promoted, there was a profound need to conduct more WRF-Chem-LES simulations to investigate the performance of our framework in as many and as complex environments as possible.

Besides, the second tier of our framework observed strong methane vestiges (i.e., likely plume tails) above the storage tanks in the Burgan field. We required to confirm that such vestiges were caused by the real plumes or the technical noises due to the surface albedo perturbations. As abovementioned, the latter had been corrected in the matched-filtered algorithm used in the second tier of our framework. To make our results more persuasive, we retrieved the PRISMA-based $\mathbf{\Delta XCH_4}$ together with surface albedo from just two spectral measurements, one featuring methane absorption (i.e., 2300 nm) and one not (i.e., 1700 nm). These two adjacent spectral bands were sufficiently close to have similar surface and aerosol reflectance properties but differed in their methane absorption properties. Specifically, we utilized these two spectral bands to launch the matched-filtered algorithm separately. The differences in the results would, in principle, eliminate surface albedo effects and thus isolate the signals of the methane plumes. Figure S13 shows that 2300 nm -driven matched-filtered algorithms resulted in noticeable methane vestiges above the storage tanks, while 1700 nm-driven algorithms did not find such signals. Therefore, we could infer that such signals may very well led by real methane plumes rather than technical noises, although on-site measurements were absent. Similar multi-spectral techniques have been widely used to retrieve signals of methane plumes from ground-based[6], airborne[7,8], and satellite-based[9,10] remote sensing instruments.

2. Detailed uncertainty analysis for the PRISMA-based methane retrievals

Methane retrievals from the PRISMA-based measurements presented systematic and random errors. Such errors were assessed by sensitivity analysis based on end-to-end simulations. At first glance via the top-of-atmosphere radiance at 2300 nm (Fig. S5), the cases in the Rumaila (Iraq) and Hassi Messaoud (Algeria) fields represented a preferable condition with a bright and homogeneous surface feature, while the cases in the Burgan (Kuwait) and Wattenberg (the United States) fields represented a challenging condition because of a relatively dark and heterogeneous surface. By comparison, the case in Yangquan (China) was even more challenging, in which mountainous areas existed. In the most cases (except for the case in Fig. 1d4), the methane plumes were clearly uncorrelated with the surface brightness from space.

Figure S10 shows the maps of the resulting methane enhancements ($\Delta\mathbf{XCH4}$) for the 1000 ~ 6000 kg/h emission sources over the plumes over the detected methane super-emitters. It was immediately clear that surface characteristics affected our retrievals strongly. For instance, at least the 1000 kg/h plumes would be needed for detection over a Burgan site (Fig. 1b3), and even higher than 2000 kg/h for a Hassi Messaoud site (Fig. 1e2). In addition, we found notable impacts of surface features on the PRISMA-based methane retrievals, which generated noise and false positives and can be eliminated by introducing the top-of-atmosphere radiance at 2300 nm (Fig. S5).

Figure S11 shows corresponding retrieval errors. Such errors denoted not only those caused by surface structures via absorption features of SWIR bands but also those due to random measurement noise. They were indicated by probability distribution functions generated by running the retrieval over a simulated image devoid of methane plumes (i.e., emission rate equal to 0 kg/h). As a result, we found that these errors roughly flowed Gaussian distributions, likely due to the fact that random noise, rather than systematic noise driven by surface structures, dominated the whole errors. This again indicates a strong dependence of the retrieval error and subsequent plume detection limit on the surface feature.

Figure S12 represents more quantitative uncertain analysis for the retrieval performance. For each case, the input $\Delta\mathbf{XCH4}$ maps were compared with the output $\Delta\mathbf{XCH4}$ retrievals. Overall, they were sketchily consistent in terms of the slopes. The retrieval method performed the best for most of the cases, with a substantial number of pixels above the noise level, while more dispersed scatters were found in the Yangquan case (Fig. 1g2). The root mean squared errors (RMSE) could be controlled within the range of 37 ~ 127 ppb. Collectively, we did not observe systematic errors in this instrument and our algorithm (Fig. S6 and Figs. S10 and S11).

3. Detailed uncertainty analysis for the TROPOMI-based methane emission estimates

We provided independent evaluations for the IME-based emission estimates of the methane hotspots using the WRF-Chem model. Table S2 summarizes the differences in the methane emission estimates from these two different methods. The results from the WRF-Chem model were consistently lower than those from the IME method in an acceptable range (23 ~ 39%). Such divergencies could be narrowed to a large extent (17 ~ 34%) once the wind data in these two methods were unified to the WRF-Chem-based wind fields. This indicates the noticeable impacts of wind information on the IME method. Besides, we also found the inevitable uncertainties in the complex physical functions in the WRF-Chem model. A representative was that the WRF-Chem-based results accounted for the wind direction that, in contrast, was not considered in the IME method.

4. Detailed uncertainty analysis for the PRISMA-based methane emission estimates

We applied the WRF-Chem-LES model to provide independent evaluations for the PRISMA-based methane emission estimates. The differences between the WRF-Chem-LES-based and IME-based results reflected the intrinsic uncertainties in the IME method. Table S3 presents the summary of the results. Overall, such differences could be controlled within -70%. Such divergencies were also mainly contributed by the differences in the wind fields between the WRF-LES-based results and the ERA5 reanalysis dataset. Yet, since all of the wind information was model product, we cannot know if the WRF-LES-based results were more reliable than the ERA5 reanalysis data. In theory, we could project that the WRF-LES-based results at a higher resolution might have a better performance.

On this basis, the IME method can be constrained by the simulated and reanalyzed (as before) wind data separately. The resulting differences reflected the impacts of wind speed on the IME method. As shown in Table S3, such differences reached up to -49%, which was within the precision errors of the IME method, as illustrated above. Besides, the comparison of the IME-based and WRF-Chem-LES results driven by the same simulated wind fields demonstrated that there were also strong uncertainties in the particular methane emission estimating method. Such uncertainties had an impact as high as that from the wind fields and, still, were not beyond uncertainties in the IME method.

Collectively, the results verified large methane emissions as reported in this work. The associated uncertainties were mainly due to wind fields and intrinsic model errors and can be controlled within -70%. It should be noted that our uncertain analysis might be only suitable for the cases in this work and more quantitative assessments based on the WRF-LES model are necessary to be promoted widely.

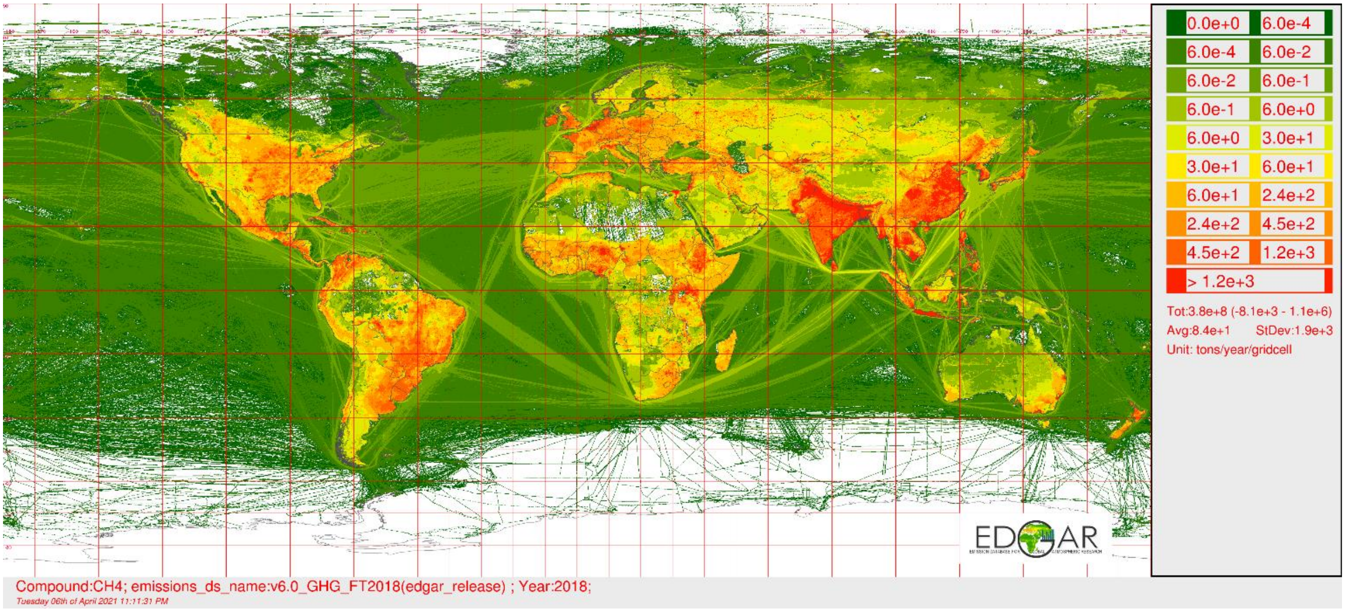

Fig. S1. A state-of-the-art global methane emission map for 2018[11]**.** The map was obtained from the EDGARv6.0 dataset (https://edgar.jrc.ec.europa.eu/gallery?release=v60ghg&substance=CH4&sector=TOTALS) (Last access: February 1, 2022).

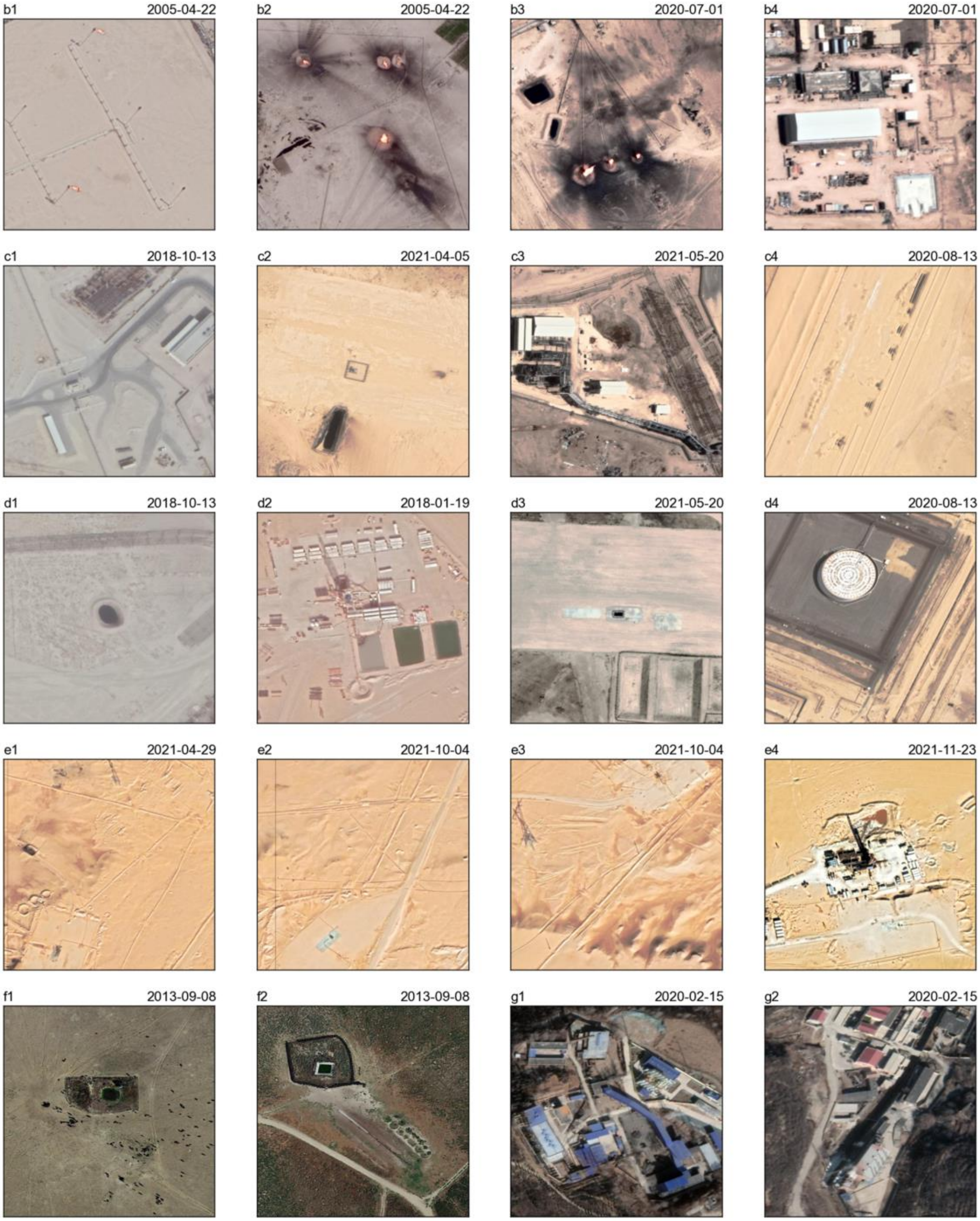

Fig. S2. Attributions of the PRISMA-based methane plumes to specific plants or infrastructures. The subpanels successively correspond to the plumes in Figs. 1b1 ~ 1g2. For each plume, the map is zoomed to the maximum for visual inspections. The overpass times of the satellites are also presented. The base maps are obtained from © Google Map.

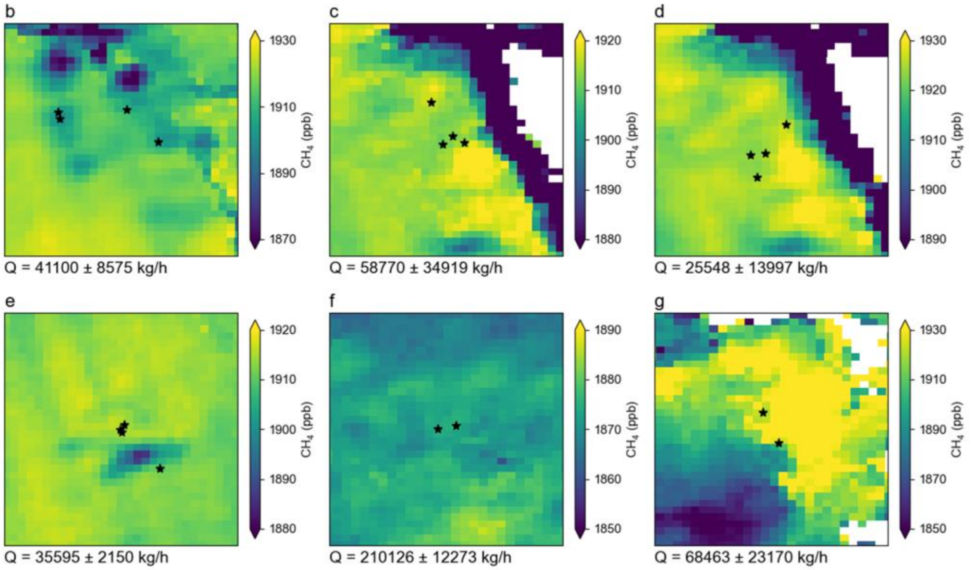

Fig. S3. The same as Figs. 1b ~ 1g but the sampling window of the first-tiered monitoring is extended to one year. The panel (c) shows the one-year average for 2020, while other panels for 2021. The five-pointed stars correspond to the black dots in Fig. 1a. The oversampling technique (3×3 km^2) is used to fuse long-term TROPOMI-based methane retrievals[12,13].

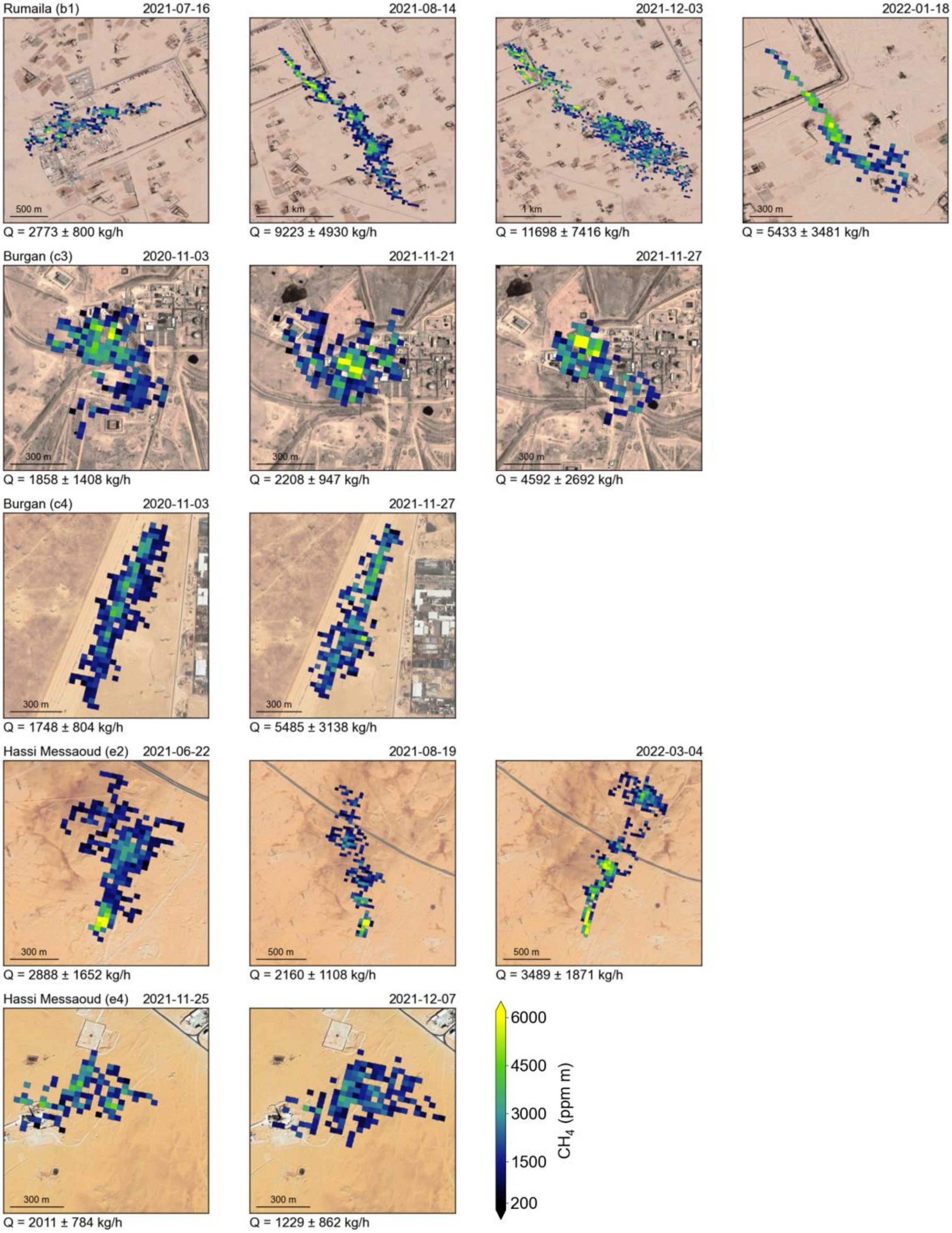

Fig. S4. The same as Figs. 1b1, c3, c4, e2, and e4 but the sampling window of the second-tiered monitoring is extended. On this basis, more representatives are presented. The base maps are obtained from © Google Map.

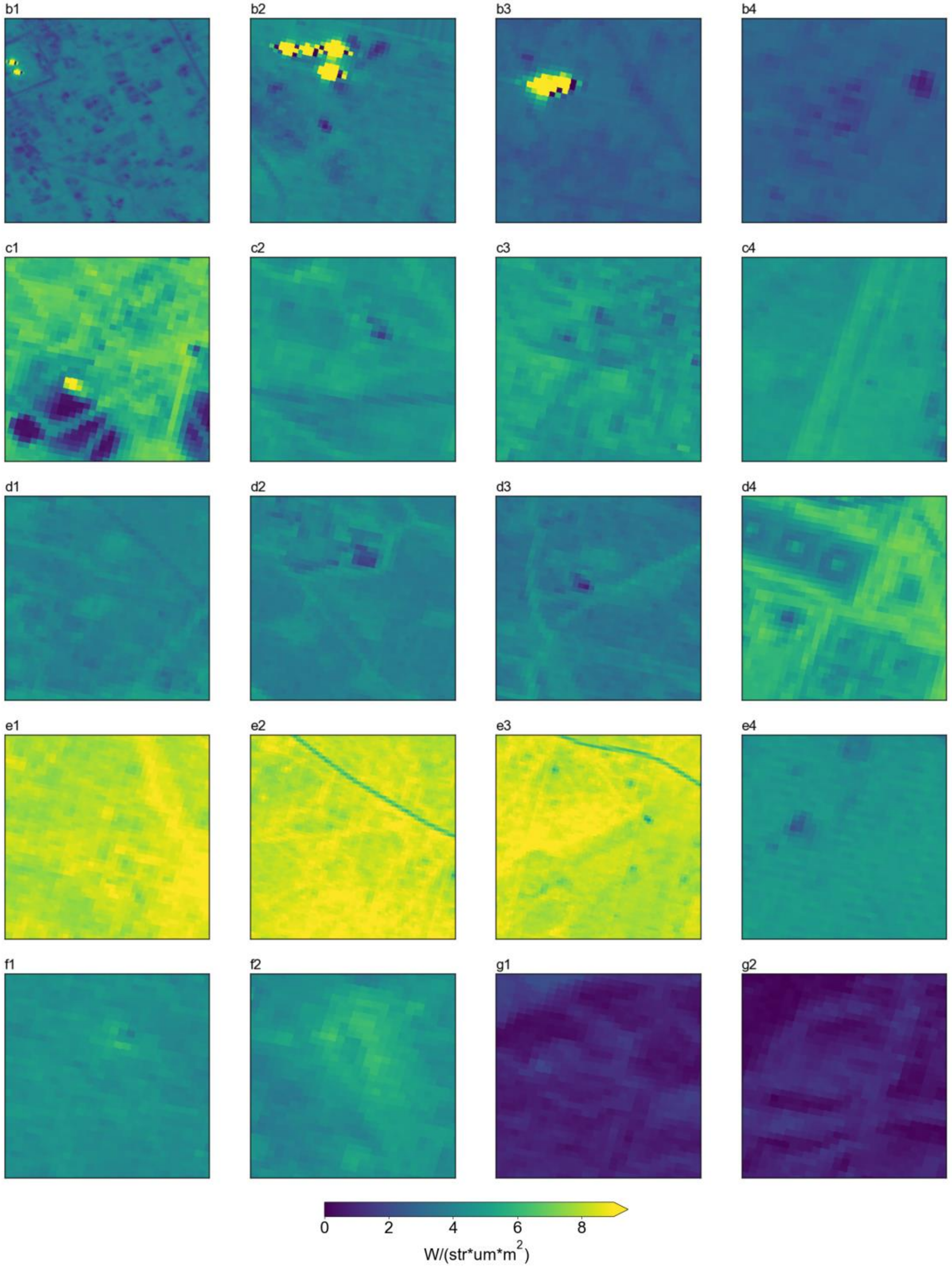

Fig. S5. Maps of top-of-atmospheric radiance at 2300 nm for the methane plumes as shown in Figs. 1b ~ 1f. The small panels confirm that spatial distributions of methane plumes were clearly uncorrelated with those of surface brightness.

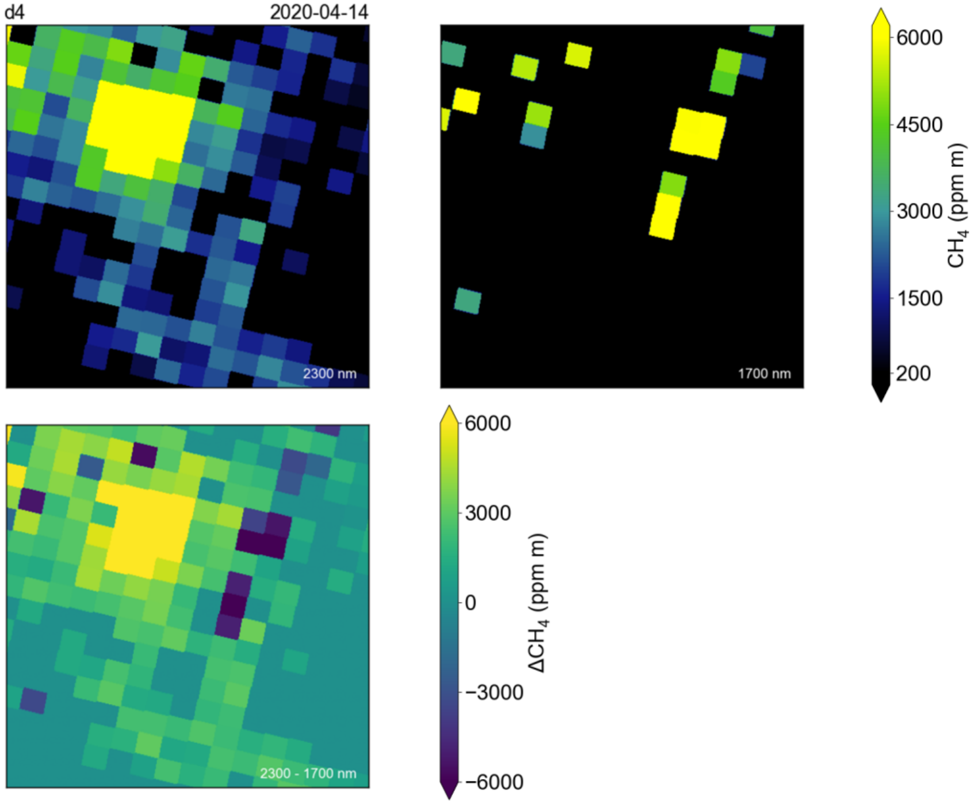

Fig. S6. Methane vestiges above the storage tanks in the Burgan field retrieved by (a) 1700 nm- and (b) 2300 nm -driven matched-filtered algorithms. Their differences highlight the suspect methane leakage from the storage tanks (c).

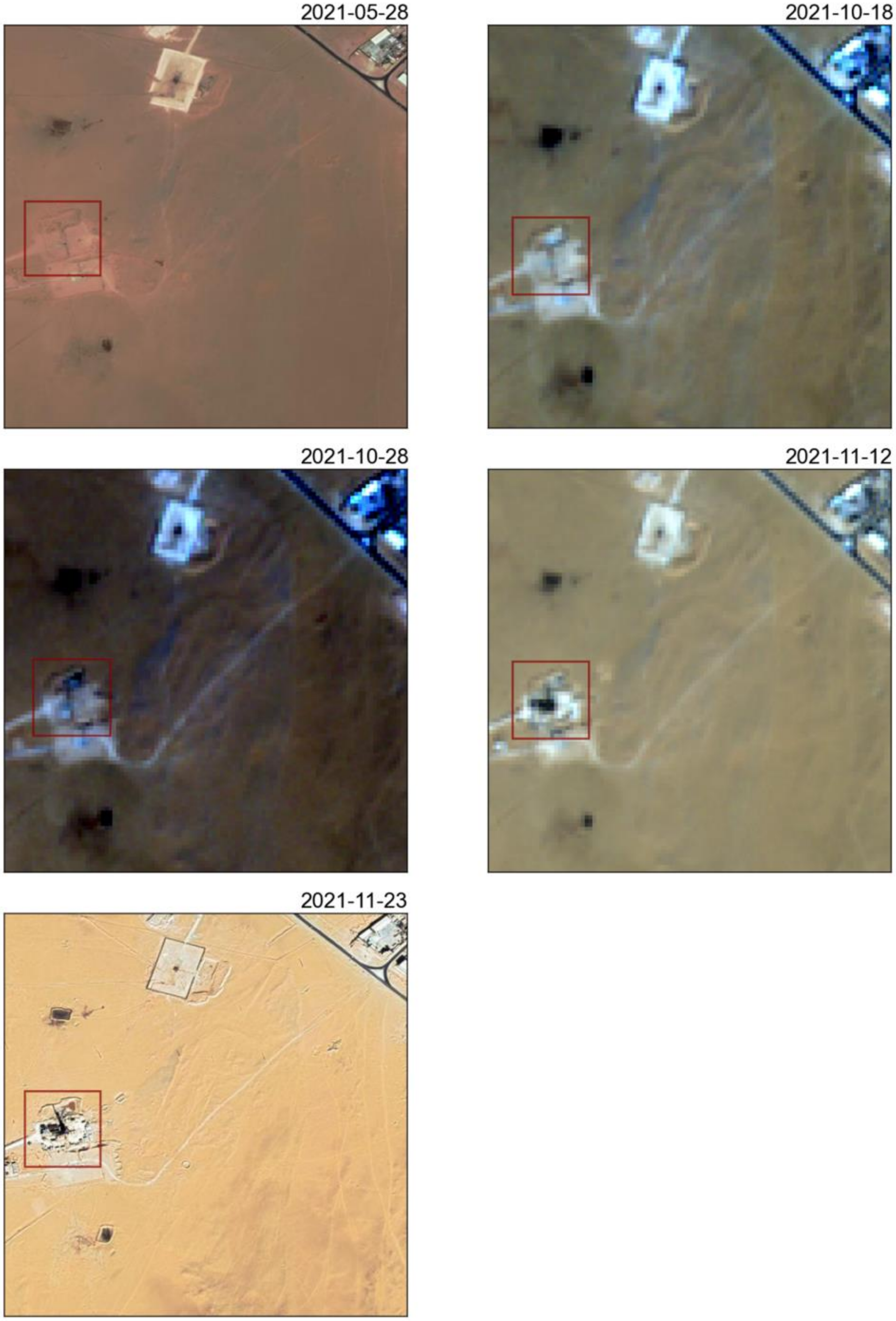

Fig. S7. Historical maps of methane plumes in the Hassi Messaoud field (Fig. 1e4). The satellite images for October 18th, October 28th, and November 12th are obtained from the Sentinel-2 images, while others © Google Map. The red rectangle marks the new methane super-emitter.

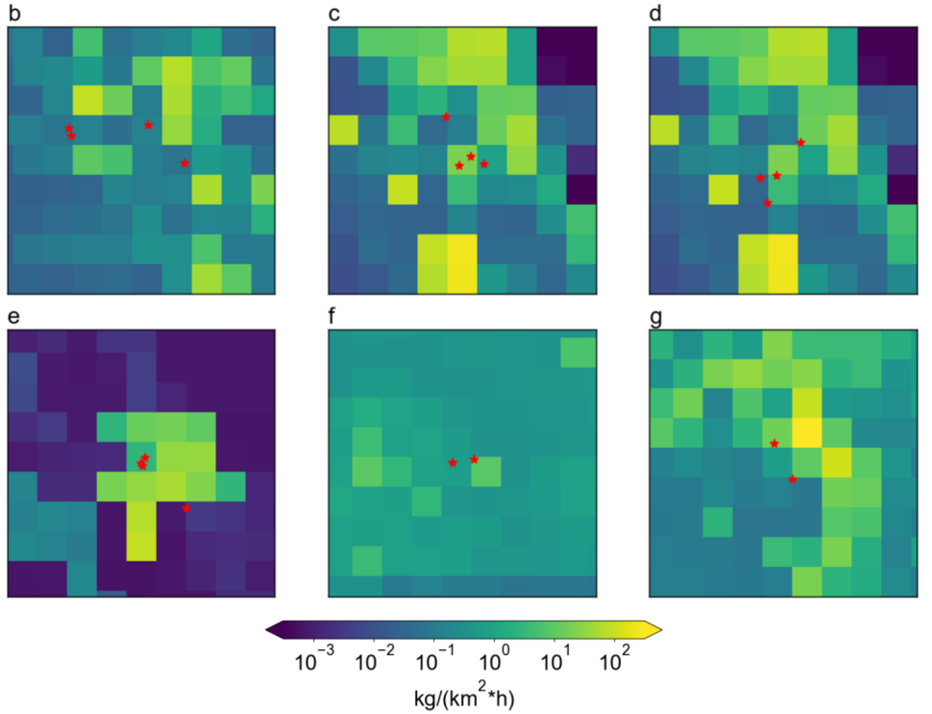

Fig. S8. Spatial distributions of methane emissions in bottom-up emission inventories. The panels successively correspond to the regions in Figs. 1b ~ 1g. The five-pointed stars correspond to the black dots in Fig. 1a.

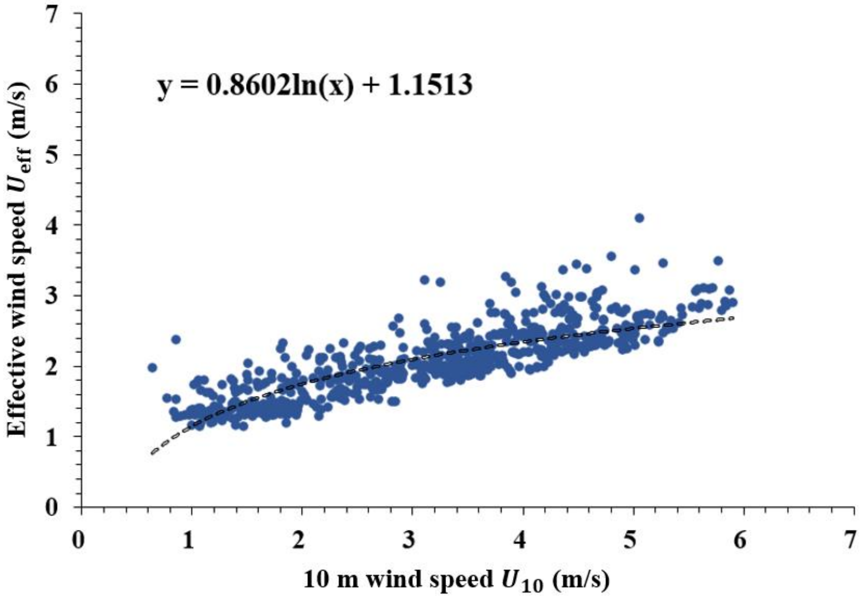

Fig. S9. Relationship between the effective (U_{eff}) and 10-m (U_{10}) wind speeds in the second-tiered monitoring. The LES plumes assuming 5% instrument precision.

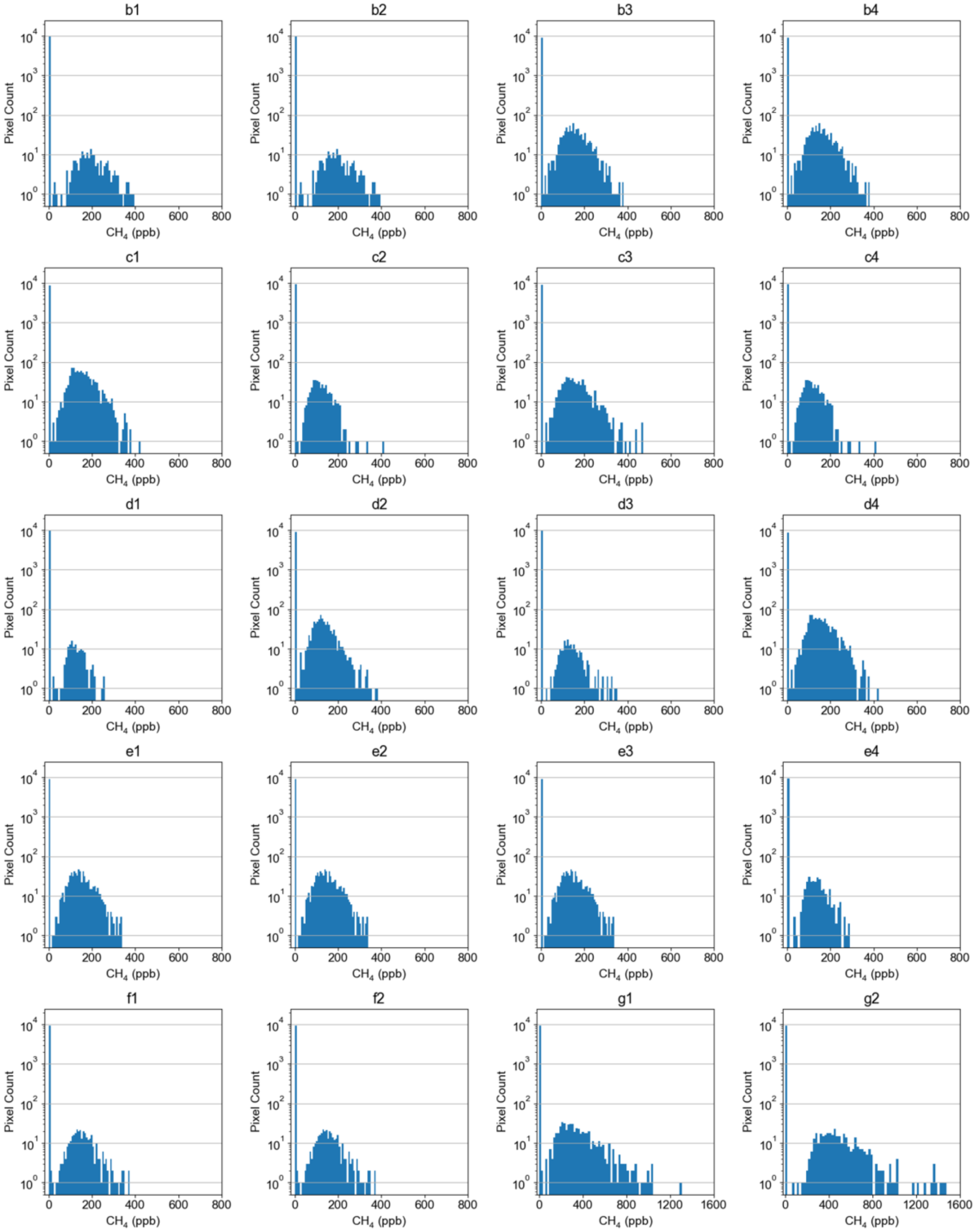

Fig. S10. Histograms of the retrieved ΔXCH4 inside the selected 100 × 100 subset areas over the detected methane super-emitters for the no-plume cases. The $\boldsymbol{\mu}$ and $\boldsymbol{\sigma}$ values represent the mean and standard deviation of the distributions, respectively. A Gaussian curve has been fitted to each distribution.

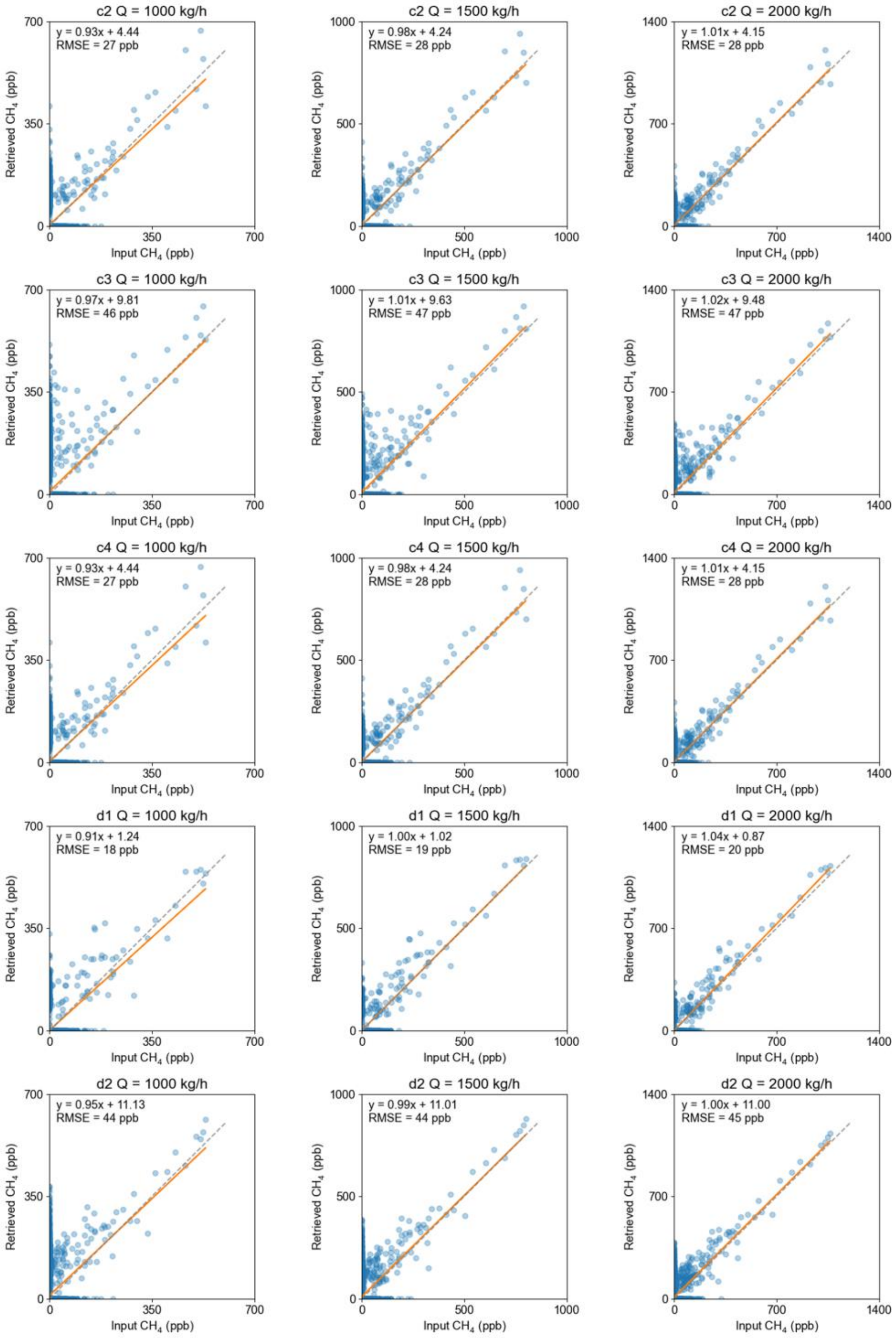
c2 Q = 1000 kg/h
y = 0.93x + 4.44
RMSE = 27 ppb
c2 Q = 1500 kg/h
y = 0.98x + 4.24
RMSE = 28 ppb
c2 Q = 2000 kg/h
y = 1.01x + 4.15
RMSE = 28 ppb
c3 Q = 1000 kg/h
y = 0.97x + 9.81
RMSE = 46 ppb
c3 Q = 1500 kg/h
y = 1.01x + 9.63
RMSE = 47 ppb
c3 Q = 2000 kg/h
y = 1.02x + 9.48
RMSE = 47 ppb
c4 Q = 1000 kg/h
y = 0.93x + 4.44
RMSE = 27 ppb
c4 Q = 1500 kg/h
y = 0.98x + 4.24
RMSE = 28 ppb
c4 Q = 2000 kg/h
y = 1.01x + 4.15
RMSE = 28 ppb
d1 Q = 1000 kg/h
y = 0.91x + 1.24
RMSE = 18 ppb
d1 Q = 1500 kg/h
y = 1.00x + 1.02
RMSE = 19 ppb
d1 Q = 2000 kg/h
y = 1.04x + 0.87
RMSE = 20 ppb
d2 Q = 1000 kg/h
y = 0.95x + 11.13
RMSE = 44 ppb
d2 Q = 1500 kg/h
y = 0.99x + 11.01
RMSE = 44 ppb
d2 Q = 2000 kg/h
y = 1.00x + 11.00
RMSE = 45 ppb
Retrieved CH4 (ppb)
Input CH4 (ppb)
0
350
700
500
1000
1400

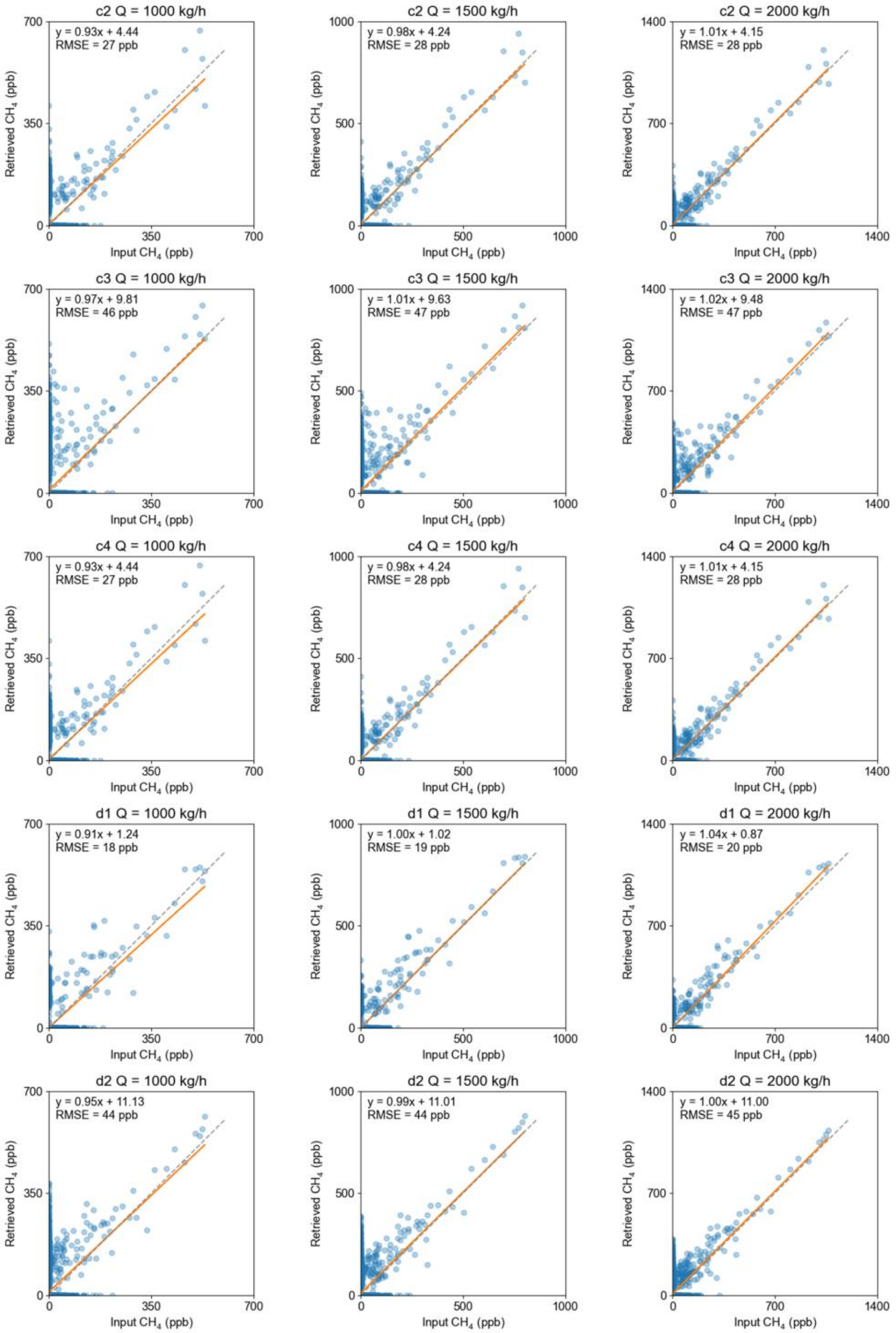
c2 Q = 1000 kg/h
y = 0.93x + 4.44
RMSE = 27 ppb
c2 Q = 1500 kg/h
y = 0.98x + 4.24
RMSE = 28 ppb
c2 Q = 2000 kg/h
y = 1.01x + 4.15
RMSE = 28 ppb
c3 Q = 1000 kg/h
y = 0.97x + 9.81
RMSE = 46 ppb
c3 Q = 1500 kg/h
y = 1.01x + 9.63
RMSE = 47 ppb
c3 Q = 2000 kg/h
y = 1.02x + 9.48
RMSE = 47 ppb
c4 Q = 1000 kg/h
y = 0.93x + 4.44
RMSE = 27 ppb
c4 Q = 1500 kg/h
y = 0.98x + 4.24
RMSE = 28 ppb
c4 Q = 2000 kg/h
y = 1.01x + 4.15
RMSE = 28 ppb
d1 Q = 1000 kg/h
y = 0.91x + 1.24
RMSE = 18 ppb
d1 Q = 1500 kg/h
y = 1.00x + 1.02
RMSE = 19 ppb
d1 Q = 2000 kg/h
y = 1.04x + 0.87
RMSE = 20 ppb
d2 Q = 1000 kg/h
y = 0.95x + 11.13
RMSE = 44 ppb
d2 Q = 1500 kg/h
y = 0.99x + 11.01
RMSE = 44 ppb
d2 Q = 2000 kg/h
y = 1.00x + 11.00
RMSE = 45 ppb
Retrieved CH$_4$ (ppb)
Input CH$_4$ (ppb)
0
350
700
500
1000
1400

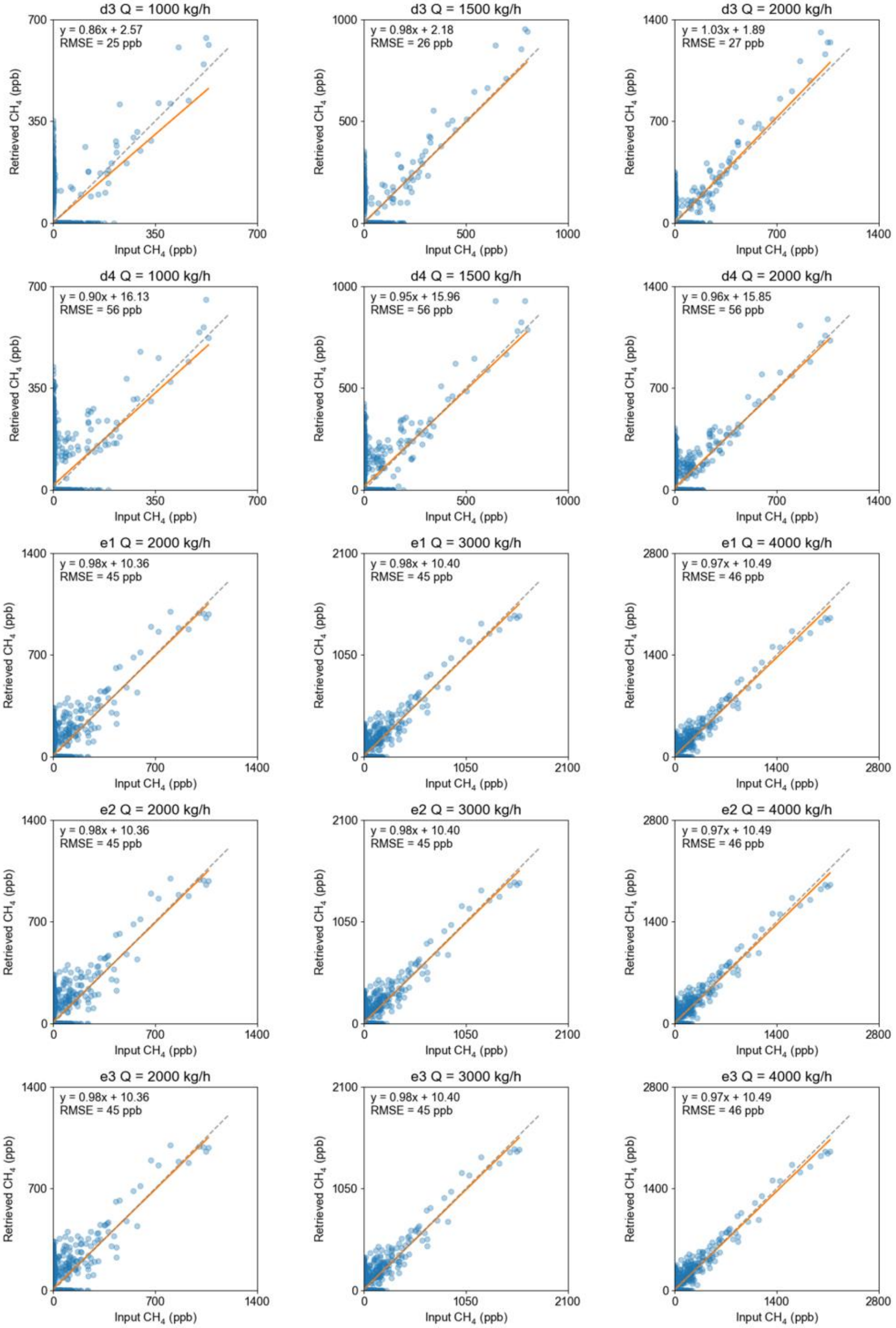

Fig. S11. Scatter plots of the input and retrieved ΔXCH4 for the simulations over the methane super-emitters. The dash and red lines represent the 1:1 line and fitted linear model, respectively.

Table S1. Summary of methane hotspots and associated super-emitters via our multi-tiered, space-based framework. Their emission rates, precision errors, locations (latitude and longitude), and corresponding figure panels are shown.

Regions	Figure panels	Latitude (°)	Longitude (°)	Emission rates kg/h	Precision errors kg/h
Rumaila	b	30.300	47.580	46138	17580
Rumaila	b1	30.291	47.725	11698	7416
Rumaila	b2	30.416	47.604	5053	3961
Rumaila	b3	30.406	47.336	6569	4009
Rumaila	b4	30.382	47.345	1510	722
Burgan	c	29.000	48.000	7873	3509
Burgan	c1	28.980	47.989	1378	992
Burgan	c2	29.013	48.027	1543	831
Burgan	c3	29.145	47.943	1858	1408
Burgan	c4	28.988	48.072	1748	804
Burgan	d	29.000	48.000	6332	3954
Burgan	d1	28.947	47.978	1375	1067
Burgan	d2	28.855	47.946	3576	1495
Burgan	d3	28.940	47.921	4425	2653
Burgan	d4	29.058	48.057	3593	2541
Hassi Messaoud	e	31.780	6.000	127676	59470
Hassi Messaoud	e1	31.798	6.012	2757	1297
Hassi Messaoud	e2	31.779	5.998	2160	1108
Hassi Messaoud	e3	31.769	6.003	4326	2453
Hassi Messaoud	e4	31.628	6.151	1229	862
Wattenberg	f	40.430	-104.380	4805	2201
Wattenberg	f1	40.443	-104.341	2023	867
Wattenberg	f2	40.430	-104.412	1142	486
Yangquan	g	37.800	113.520	33594	16918
Yangquan	g1	37.746	113.551	7616	4413
Yangquan	g2	37.866	113.489	4382	2034

Table S2. Comparison of the TROPOMI-based methane emission estimates between the IME and WRF-Chem method.

Figure	IME (kg/h)	WRF-Chem (kg/h)	IME-Wind* (kg/h)	（WRF-Chem - IME)/IME (%)	（IME-Wind - IME)/IME (%)
b	46138	32758	36449	-29	-21
c	7873	5117	5589	-35	-29
d	6332	3863	4179	-39	-34
e	127676	77882	105971	−39	-17
f	4805	3700	4036	-23	-16
g	33594	23516	24859	-30	-26

*IME-Wind: the wind data in the IME method is constrained by the WRF-Chem model.

Table S3. Comparison of the PRISMA-based methane emission estimates between the IME and WRF-Chem-LES method.

Figure	IME (kg/h)	WRF-Chem-LES (kg/h)	IME-Wind* (kg/h)	（WRF-Chem-LES - IME)/IME (%)	（IME-Wind - IME)/IME (%)
b1	11698	5381.08	6784.84	-54	-42
b2	5053	1869.61	3840.28	-63	-24
b3	6569	3021.74	4926.75	-54	-25
b4	1510	815.4	906	-46	-40
c1	1378	454.74	1005.94	-67	-27
c2	1543	972.09	972.09	-37	-37
c3	1858	743.2	873.26	-60	-53
c4	1748	1136.2	1293.52	-35	-26
d1	1375	467.5	756.25	-66	-45
d2	3576	2467.44	2717.76	-31	-24
d3	4425	2566.5	3363	-42	-24
d4	3593	1113.83	1832.43	-69	-49
e1	2757	1792.05	1847.19	-35	-33
e2	2160	1188	1576.8	-45	-27
e3	4326	2509.08	2811.9	-42	-35
e4	1229	516.18	749.69	-58	-39
f1	2023	1456.56	1537.48	-28	-24
f2	1142	787.98	833.66	-31	-27
g1	7616	4569.6	5483.52	-40	-28
g2	4382	2935.94	3067.4	-33	-30

*IME-Wind: the wind data in the IME method is constrained by the WRF-Chem model.

Reference.

[1] Varon DJ, Jacob DJ, McKeever J, Jervis D, Durak BOA, Xia Y, et al. Quantifying methane point sources from fine-scale satellite observations of atmospheric methane plumes. Atmos Meas Tech 2018;11:5673–86. https://doi.org/10.5194/amt-11-5673-2018.

[2] Wang L, Yu S, Li P, Chen X, Li Z, Zhang Y, et al. Significant wintertime PM$_\mathbf{2.5}$ mitigation in the Yangtze River Delta, China from 2016 to 2019: observational constraints on anthropogenic emission controls. Atmos Chem Phys Discuss 2020;2020:1–31. https://doi.org/10.5194/acp-2020-510.

[3] Wang L, Chen X, Zhang Y, Li M, Li P, Jiang L, et al. Switching to electric vehicles can lead to significant reductions of PM2.5 and NO2 across China. One Earth 2021;4:1037–48. https://doi.org/https://doi.org/10.1016/j.oneear.2021.06.008.

[4] Itziar I-L, Luis G, Yin-Nian L, J. VD, D. MJ, Yuzhong Z, et al. Satellite-based survey of extreme methane emissions in the Permian basin. Sci Adv 2021;7:eabf4507. https://doi.org/10.1126/sciadv.abf4507.

[5] Mehmood K, Wu Y, Wang L, Yu S, Li P, Chen X, et al. Relative effects of open biomass burning and open crop straw burning on haze formation over central and eastern China: Modeling study driven by constrained emissions. Atmos Chem Phys 2020;20. https://doi.org/10.5194/acp-20-2419-2020.

[6] Innocenti F, Robinson R, Gardiner T, Finlayson A, Connor A. Differential Absorption Lidar (DIAL) Measurements of Landfill Methane Emissions. Remote Sens 2017;9. https://doi.org/10.3390/rs9090953.

[7] Leifer I, Roberts D, Margolis J, Kinnaman F. In situ sensing of methane emissions from natural marine hydrocarbon seeps: A potential remote sensing technology. Earth Planet Sci Lett 2006;245:509–22. https://doi.org/https://doi.org/10.1016/j.epsl.2006.01.047.

[8] Roberts DA, Bradley ES, Cheung R, Leifer I, Dennison PE, Margolis JS. Mapping methane emissions from a marine geological seep source using imaging spectrometry. Remote Sens Environ 2010;114:592–606. https://doi.org/https://doi.org/10.1016/j.rse.2009.10.015.

[9] Varon DJ, Jervis D, McKeever J, Spence I, Gains D, Jacob DJ. High-frequency monitoring of anomalous methane point sources with multispectral Sentinel-2 satellite observations. Atmos Meas Tech 2021;14:2771–85. https://doi.org/10.5194/amt-14-2771-2021.

[10] Ehret T, Truchis A De, Mazzolini M, Morel J-M, d’Aspremont A, Lauvaux T, et al. Global Tracking and Quantification of Oil and Gas Methane Emissions from Recurrent Sentinel-2 Imagery 2021.

[11] Janssens-Maenhout G, Crippa M, Guizzardi D, Muntean M, Schaaf E, Dentener F, et al. EDGAR v4.3.2 Global Atlas of the three major greenhouse gas emissions for the period 1970–2012. Earth Syst Sci Data 2019;11:959–1002. https://doi.org/10.5194/essd-11-959-2019.

[12] Sun K, Zhu L, Cady-Pereira K, Chan Miller C, Chance K, Clarisse L, et al. A physics-based approach to oversample multi-satellite, multispecies observations to a common grid. Atmos Meas Tech 2018;11:6679–701. https://doi.org/10.5194/amt-11-6679-2018.

[13] Martin, Van, Damme, Lieven, Clarisse, Simon, et al. Industrial and agricultural ammonia point sources exposed. Nature 2018.